Supporting Information

Lilley et al. 10.1073/pnas.1321990111

SI Materials and Methods

Immunohistochemistry. Animals were transcardially perfused with Ringer's solution followed by fixative [4% (wt/vol) PFA in 0.1 M phosphate buffer at pH 7.2; PB]. After thorough washing in 0.1 M PB, tissue was incubated overnight at 4 °C in 30% wt/vol sucrose in 0.1 M PB, then was embedded in OCT medium (TissueTek) and frozen. Sections (12–20 μm) were cut on a cryostat, mounted on glass slides, and air-dried. After rehydration in Tris-buffered saline (TBS), tissue sections were incubated in blocking buffer [TBS with 10% (vol/vol) normal goat or donkey serum, 0.3% Triton X-100] for 2 h and were then incubated overnight at 4 °C with primary antibody diluted in blocking buffer. Slides were washed in TBS and incubated for 2 h at room temperature secondary antibodies diluted in blocking buffer. Following additional washes, sections were incubated with Neurotrace 435 (Invitrogen) and mounted with Vectashield (Vector Laboratories). For whole mount immunohistochemistry, diaphragm muscle was dissected out and incubated with blocking buffer for 16 h, followed by primary and secondary antibody incubations for 72 h. Washing of primary and secondary antibodies was done with five to six changes of TBS + 0.1% Triton X-100. After secondary antibody incubation, tissue was soaked in Vectashield overnight then mounted on a glass slide and coverslipped.

The following antibodies were used for immunohistochemistry: rabbit and goat anti-parvalbumin (Swant), anti-SytII mAb ZNP1, anti-PSD93 (DHSB), anti-NF-H mAb SMI312 (Covance), mouse mAb TUJ1 (Covance), rabbit mAb anti-BRSK2 (Cell Signaling Technologies), chicken anti-GFP, guinea pig anti-VGLUT1, goat anti-ChAT, rabbit anti-synaptophysin, guinea pig anti VAchT (Millipore). Dye-conjugated secondary antibodies and α-bungarotoxin (BTX) were from Invitrogen.

Images were obtained with an Olympus FV1000 confocal microscope as described (1). ImageJ was used to analyze confocal stacks and generate maximum intensity projections. Images were processed in Adobe Photoshop. Imaris v7.3 was used for quantitative analysis of synapse size and number by using the Surfaces function. The area of BTX reactivity and the volume of synaptophysin and VGLUT1 boutons were calculated for NMJ, SCG, and Ia-MN synapses, respectively. For quantification of Calyx of Held occupancy, confocal stacks were acquired with a 60× 1.45 N.A. objective and were imported into ImageJ. The equators of median nucleus of the trapezoid body (MNTB) neuronal somata were outlined by using the freehand draw tool by delimiting the area that was parvalbumin (PV) positive but VGLUT1/SytII negative. Areas of synaptic occupancy were identified as VGLUT1/SytII/PV-positive areas that were apposed to the somata. Fractional occupancy was calculated by dividing the total linear distance of apposed regions by the circumference of the MNTB somata. All data used for quantification were from a minimum of four animals from three different litters. GraphPad Prism was used for data analysis and for statistical tests indicated.

Electrophysiology. For extracellular compound action potential (CAP) recordings, ganglia were rapidly dissected, pinned down in a recording chamber, and perfused continuously at ∼5 mL/min with oxygenated Ringer's solution at room temperature. The preganglionic nerve in the cervical sympathetic trunk was connected to a battery-powered stimulator with a suction electrode. The postganglionic trunk was connected to a multiclamp 700B (Molecular Devices) with a suction electrode; CAPs were amplified, filtered at 100 Hz and 1 kHz, digitized with an Axon DigiData 1400 (Molecular Devices), and stored on a personal computer running pClamp (Molecular Devices). Data were converted to general binary files and analyzed off-line with Igor Pro (WaveMetrics). All drugs were added directly to the oxygenated Ringer's solution. Experiments were performed without prior knowledge of the genotypes of the animals used.

Intracellular recordings from motor neurons were made from control and mutant postnatal day (P)5–P7 animals as described (2). A Na^+-channel blocker (500 mM QX-314) was added to the microelectrodes to block antidromic action potentials; the failed action potentials are visible just before the synaptic responses in Fig. 6*C*. The specificity index for EPSPs in identified motor neurons evoked by muscle nerve stimulation (Fig. S8*H*) was determined as described (2). For extracellular recordings of responses in motor neurons to stimulation of sensory axons in dorsal roots (Fig. S8*D*), synaptic potentials (sometimes including orthodromic action potentials) were recorded from the cut L4 ventral roots with tight-fitting suction electrodes. A total of 18 nonlittermate animals of control, $SAD^{Isl1\text{-}cre}$, and $SAD^{PV\text{-}cre}$ genotypes were used for all of these experiments.

Electron Microscopy. Methods for tissue preparation, sectioning, and imaging were carried out as described in ref. 4. Briefly, superior cervical ganglia and small pieces of diaphragm (containing nerve and NMJs) were rapidly removed and placed in fixative (4% wt/vol paraformaldehyde, 2% wt/vol glutaraldehyde in 0.1 M phosphate buffer) for 2 h. Tissue was then cut into 1- to 2-mm pieces and placed into fresh fixative for 4 h followed by thorough washing with sodium cacodylate buffer and postfixation with 2% osmium tetroxide for 1 h. Samples were washed with double distilled water three times for 3 min each and were dehydrated by using a graded ethanol solution (50%, 70%, 80%, 90%, 95%, 100% for 5 min each) followed by immersion in propylene oxide. Tissue was then infiltrated with epon resin by using a schedule of 3:1 (propylene oxide:resin) for 1 h, 2:1 for 2 h, and 1:1 overnight. The next morning, tissue was placed in fresh resin and embedded. Specimens were sectioned on a Leica ultramicrotome at 50 nm and were imaged by using a Zeiss scanning electron microscope as described (3).

1. Lefebvre JL, Kostadinov D, Chen WV, Maniatis T, Sanes JR (2012) Protocadherins mediate dendritic self-avoidance in the mammalian nervous system. *Nature* 488(7412):517–521.
2. Wang Z, Li LY, Taylor MD, Wright DE, Frank E (2007) Prenatal exposure to elevated NT3 disrupts synaptic selectivity in the spinal cord. *J Neurosci* 27(14):3686–3694.
3. Tapia JC, et al. (2012) Pervasive synaptic branch removal in the mammalian neuromuscular system at birth. *Neuron* 74(5):816–829.

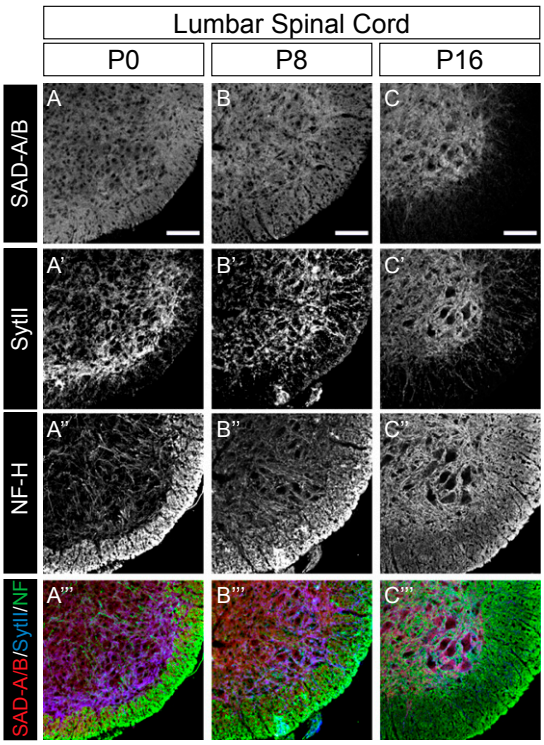

Fig. S1. Redistribution of SAD-A/B to synaptic sites during development. SAD-A/B immunohistochemistry of the ventral lumbar spinal cord shows that SADs redistribute away from axonal tracts at P0 toward synaptic sites by P16 (observe colocalization of SADs with SytII in *C* and *C′*). (Scale bars: 20 μm.)

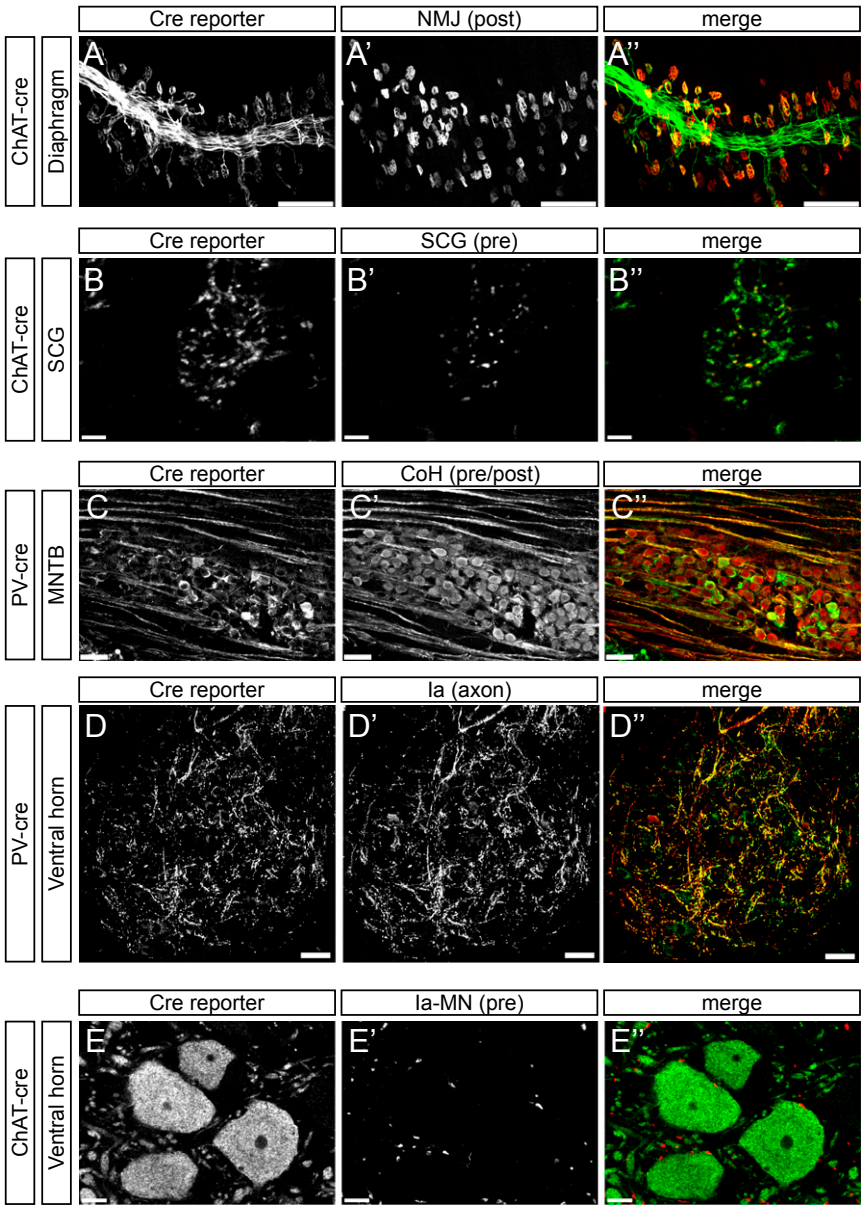

Fig. S2. Analysis of ChAT-cre and PV-cre activity in the peripheral and central nervous systems. (*A*–*B*′′) Cre reporter analysis at P8 shows that ChAT-cre is expressed by all motor neurons innervating the diaphragm (*A*–*A*′′), and by preganglionic fibers but not postsynaptic cells in the SCG (*B*–*B*′′). (*C*–*C*′′) Cre reporter analysis in the MNTB showing that PV-cre is active in axons that form the Calyx of Held at P6 (*C*), but has not yet turned on in MNTB principal cells (somata labeled by PV in *C*′). (*D* and *E*) Cre reporter analysis of PV-cre and ChAT-cre in the ventral horn demonstrating that PV-cre only acts in IaPSN axons (*D*–*D*′′) and ChAT-cre is active only in motor neurons (*E*–*E*′′). (Scale bars: *A*, 100 μm; *B*, 5 μm; *C* and *D*, 50 μm; *E*, 10 μm.)

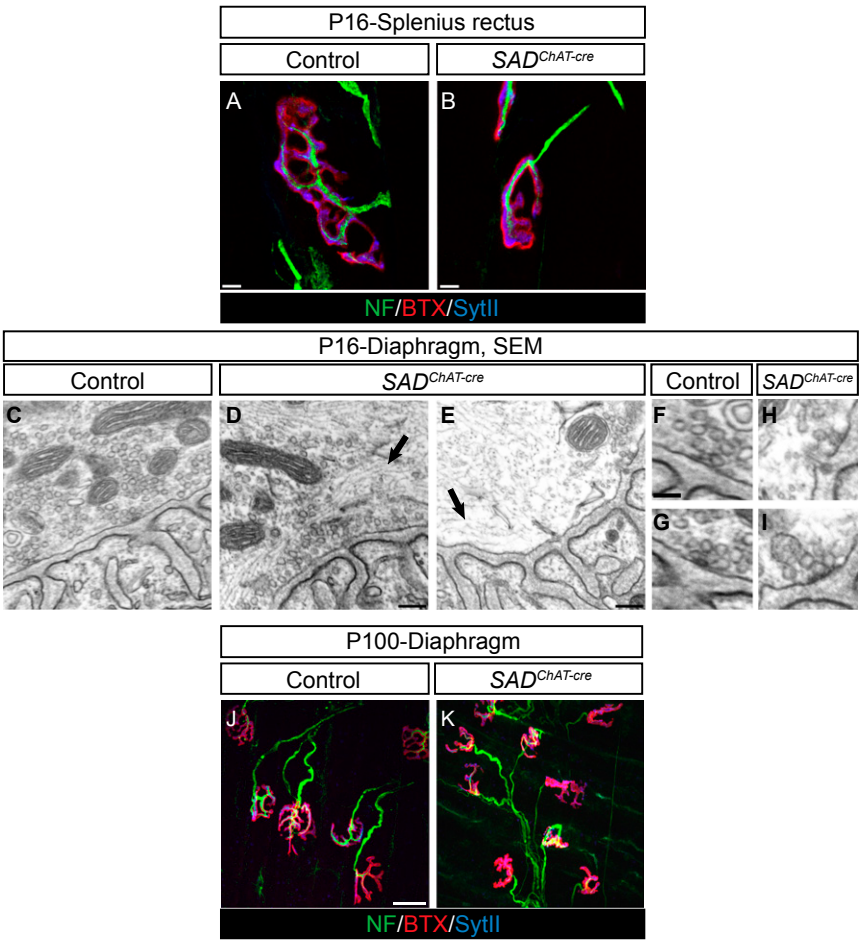

Fig. S3. Role of SAD kinases in maturation of the NMJ. (*A* and *B*) Immunohistochemistry reveals NMJ maturation defects in the splenius rectus muscle of $SAD^{ChAT\text{-}cre}$ animals similar to those shown for diaphragm in Fig. 2. (*C–E*) Electron microscopy of control and $SAD^{ChAT\text{-}cre}$ diaphragm shows the presence of filamentous material (arrows) at the presynaptic membrane that displaces synaptic vesicles from release sites adjacent to postsynaptic folds in mutants NMJs. (*F–I*) Higher magnification images of active zones in control and $SAD^{ChAT\text{-}cre}$ NMJs. (*J* and *K*) Immunohistochemistry of diaphragm muscle at P100 shows that synaptic defects seen in 1-mo-old animals (Fig. 2) persist but are not exacerbated in adulthood. (Scale bars: *A* and *B*, 5 μm; *C–E*, 200 nm; *F*, 100 nm; *J*, 20 μm.)

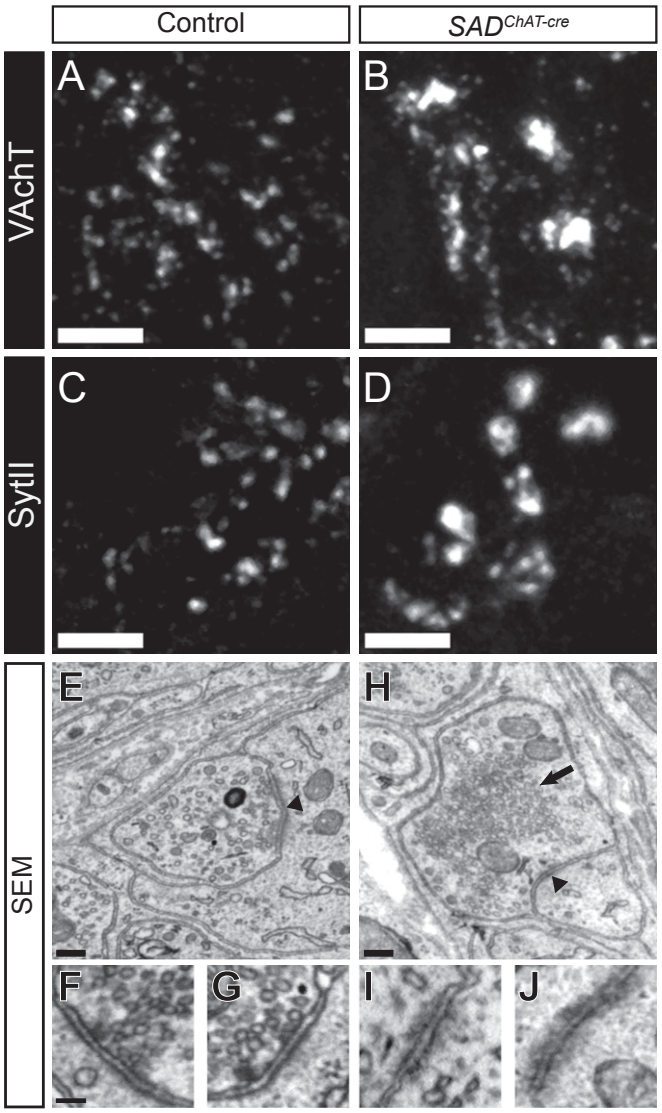

Fig. S4. Role of SAD kinases in maturation of the SCG. (*A–D*) Immunohistochemistry with presynaptic markers antivesicular acetylcholine transporter (VAChT; *A* and *B*) and anti-synaptotagmin II (SytII: *C* and *D*) shows enlargement of boutons in SAD-deficient axons. (*E* and *H*) Electron microscopic images of P16 SCG showing aggregation of synaptic vesicles (arrow) localized more than 200 nm away from a visible active zone (arrowhead) in $SAD^{ChAT\text{-}cre}$ animals. (*F*, *G*, *I*, and *J*) Higher magnification images of active zones in control and $SAD^{ChAT\text{-}cre}$ mutant SCG. (Scale bars: *D*, 5 μm; *E*, 200 nm; *F*, 100 nm.)

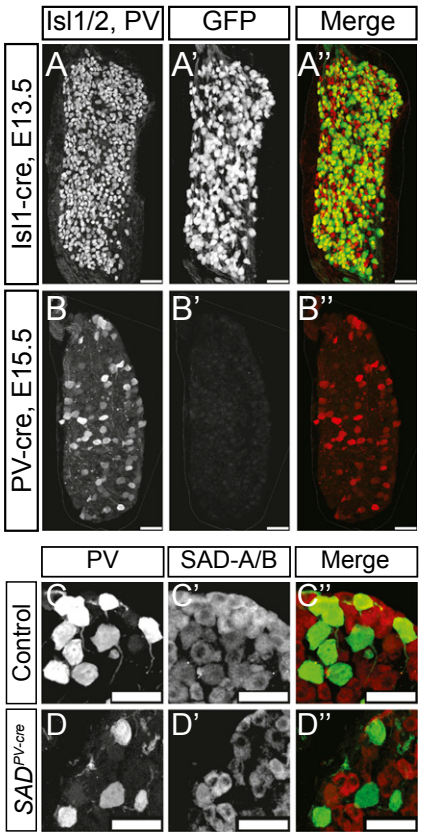

Fig. S5. Timed deletion of SAD kinases from sensory neurons using cre driver lines. (*A–B′′*) Immunohistochemistry of lumbar DRG from E13.5 Isl1-cre; Rc::Epe and E15.5 PV-cre; Rc::Epe animals showing that Isl1-cre is active by E13.5 but PV-cre is not active until after E15 (Fig. S2). (*C–D′′*) SAD-A/B immunohistochemistry of P0 lumbar DRG from control (*C–C′′*) or $SAD^{PV\text{-}cre}$ (*D–D′′*) animals demonstrating that PV-cre ablates SAD protein in PV^{+} DRG neurons. (Scale bars: 50 μm.)

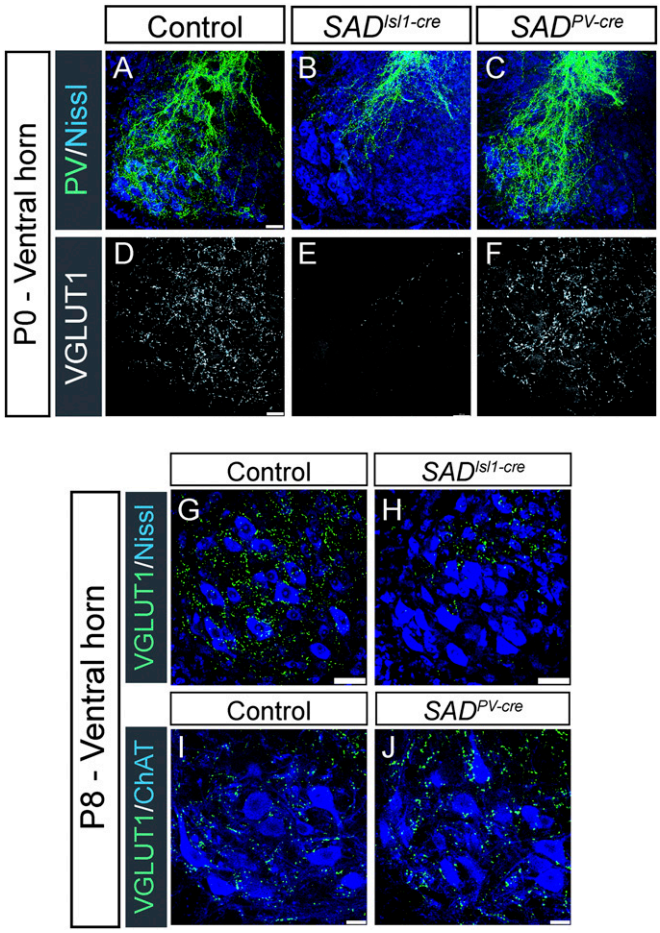

Fig. S6. SAD kinases play multiple sequential roles in the development of Ia-MN connectivity. (*A–F*) PV and VGLUT1 immunohistochemistry of P0 ventral horn. Early deletion of SADs in $SAD^{Isl1\text{-}cre}$ mice (*B* and *E*) causes IaPSN axons to terminate prematurely before reaching the ventral horn leading to a loss of $VGLUT1^{+}$ boutons adjacent to motor neurons. In contrast, later deletion in $SAD^{PV\text{-}cre}$ mice (*C* and *F*) does not affect terminal arbor formation. (*G–J*) The defect in $SAD^{Isl1\text{-}cre}$ mice persists at P8 (*H*), whereas $VGLUT1^{+}$ boutons assemble on motor neurons in $SAD^{PV\text{-}cre}$ mice (*J*). (Scale bars: *A–C*, 50 μm; *D–F*, 20 μm; *G–J*, 50 μm.)

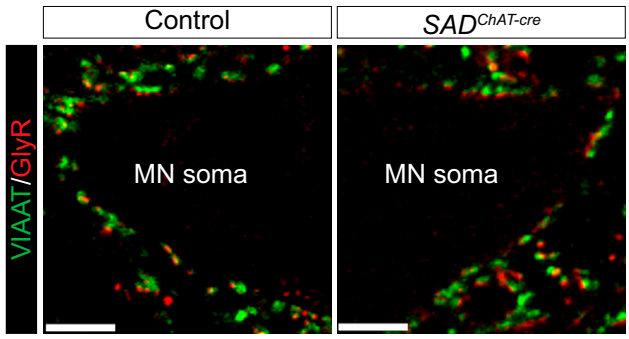

Fig. S7. Inhibitory synapses form on SAD-deficient motor neurons. Immunohistochemistry of P16 ventral horn with antibodies for VIAAT and Glycine receptors showing apposition of inhibitory synaptic markers on the somata of motor neurons in control (*Left*) and $SAD^{ChAT\text{-}cre}$ (*Right*) animals. (Scale bars: 5 μm.)

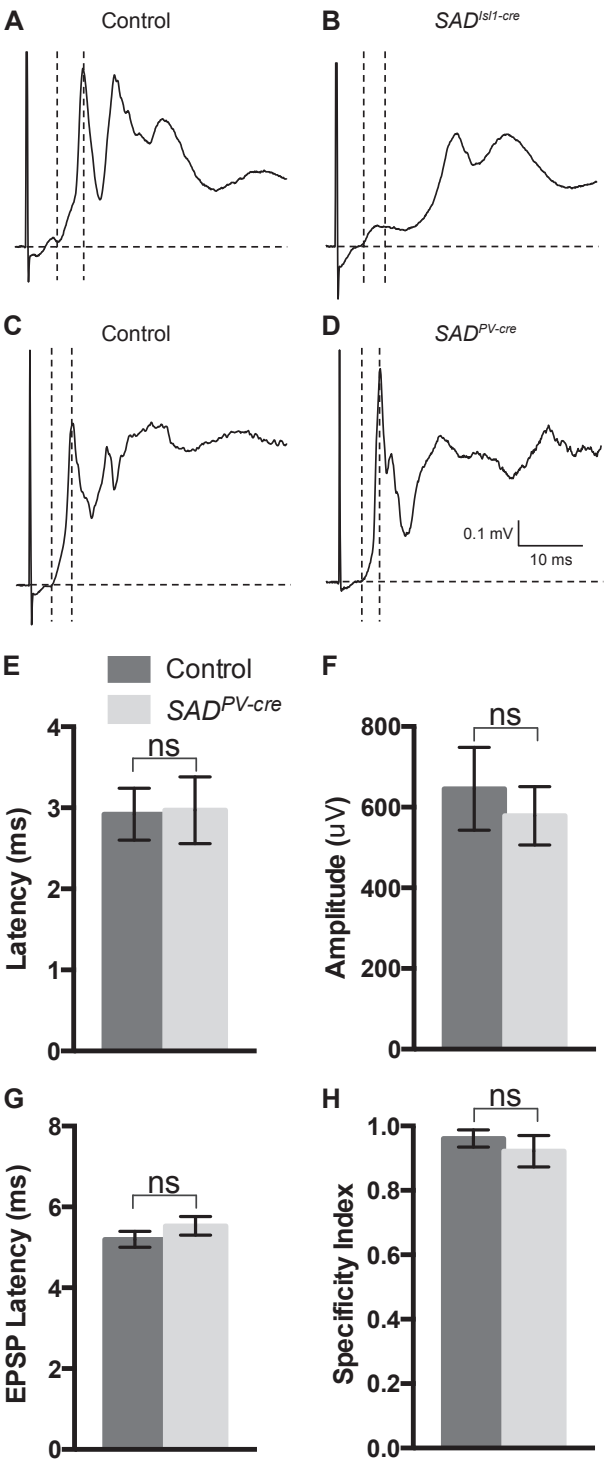

Fig. S8. SAD kinases are required for functional maturation of sensory-motor synapses in the spinal cord. (*A* and *B*) Sample traces of L4 ventral root (VR) recordings following L4 dorsal root (DR) stimulation from control and $SAD^{Isl1\text{-}cre}$ animals at P0. The dotted lines delineate the latencies to the onset and peak amplitude of the monosynaptic response. Response amplitudes are strong in control animals and lead to action potential firing, but are weak in $SAD^{Isl1\text{-}cre}$ mutants. (*C* and *D*) Sample traces of L4 VR recordings as in *A* and *B* but from control and $SAD^{PV\text{-}cre}$ mice at P5–P7. The monosynaptic response is strong in both control and $SAD^{PV\text{-}cre}$ mutants. Calibration applies to *A*–*D*. (*E* and *F*) Latencies and amplitudes of L4 ventral root responses from control and $SAD^{PV\text{-}cre}$ animals at P5–P7, demonstrating that deletion of SADs with PV-cre does not significantly affect the response. ns, difference not statistically significant. (*G*) Latencies of monosynaptic homonymous EPSPs in control and $SAD^{PV\text{-}cre}$ animals were not significantly different at P5–P7 (mean ± SEM, control, $n = 14$; $SAD^{PV\text{-}cre}$, $n = 13$; unpaired t test, $P = 0.28$). (*H*) Specificity of connections was not altered in $SAD^{PV\text{-}cre}$ animals relative to controls. Specificity index was calculated as described (ref. 1; bars show mean ± SEM, control, $n = 14$; $SAD^{PV\text{-}cre}$, $n = 13$, unpaired t test: $P = 0.48$.)

1. Wang Z, Li LY, Taylor MD, Wright DE, Frank E (2007) Prenatal exposure to elevated NT3 disrupts synaptic selectivity in the spinal cord. *J Neurosci* 27(14):3686–3694.